Supplementary Material (ESI) for Chemical Communications

Using One Spin-Transition to Trigger Another in Solid Solutions of Two Different Spin-Crossover Complexes

Malcolm A. Halcrow*

School of Chemistry, University of Leeds, Woodhouse Lane, Leeds, UK LS2 9JT.
E-mail: m.a.halcrow@leeds.ac.uk

Electronic Supplementary Information

Figure S1 Partial packing diagrams of $[Fe(bpp)_2][BF_4]_2$ and $[Co(terpy)_2][BF_4]_2$, showing the "terpyridine embrace" lattice.

Table S1 Elemental microanalyses of the solid solution materials and their pure precursor compounds.

Table S2 Experimental details for the single crystal structure determination of $[Ru(bpp)_2][BF_4]_2$

Table S3 Selected bond lengths and angles in the crystal structure of $[Ru(bpp)_2][BF_4]_2$.

Figure S2 View of the complex dication in $[Ru(bpp)_2][BF_4]_2$.

Figure S3 Selected powder *X*-ray diffraction data from the compounds in this work.

Table S4 Assignment of the ES mass spectra from $[M(bpp)_2][BF_4]_2$ (M = Fe and Ru), $[Co(terpy)_2][BF_4]_2$ and the solid solutions.

Figure S4 Electrospray mass spectra of **1b** and **2b**.

Figure S5 ^{1}H NMR spectra of **1b** and **2b**.

Table S5 Predicted and observed values of $\chi_M T$ (cm^3 mol^{-1} K) from high- and low-spin **1a**-**1c** and **2a**-**2c**, based on the analytical compositions of the samples.

Figure S6 Experimental and simulated *X*-band EPR spectrum of **1a** at 113 K.

Figure S7 Low temperature *X*-band powder EPR spectra of the solid solutions in this work.

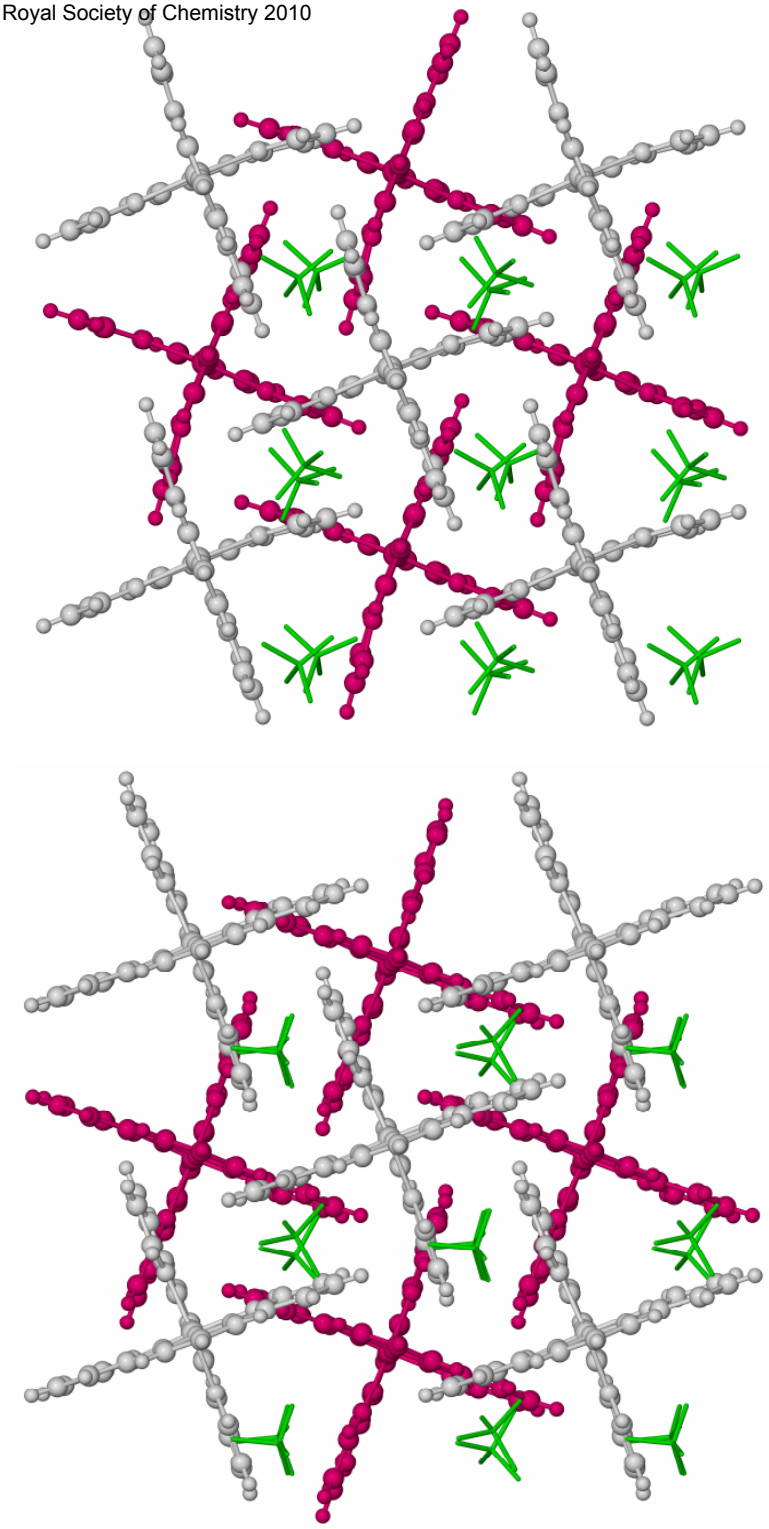

Fig. S1 Partial packing diagrams of $[Fe(bpp)_2][BF_4]_2$ (top)[11,12] and $[Co(terpy)_2][BF_4]_2$ (bottom)[13] at 300 K, showing the "terpyridine embrace" lattice. The reference numbers are the same as those used in the main paper.

Both views are parallel to the [001] crystallographic vector, with [110] ($[Fe(bpp)_2][BF_4]_2$) or [100] ($[Co(terpy)_2][BF_4]_2$) running horizontally. The complex dications in both structures associate into alternating four-fold layers, coloured white and pink. Only one orientation of the disordered BF_4^- ions is shown, which are de-emphasised and coloured green.

Table S1 Elemental microanalyses of the solid solution materials $[Fe(bpp)_2]_z[Co(terpy)_2]_{1-z}[BF_4]_2$ (**1a-1c**), $[Ru(bpp)_2]_z[Co(terpy)_2]_{1-z}[BF_4]_2$ (**2a-2c**) and their pure precursor compounds [found, % (calcd, %)]. The estimated error on *z*, based on these data, is ±0.01.

	z	C	H	N	Fe	Co
$[Fe(bpp)_2][BF_4]_2$	–	40.3 (40.5)	2.75 (2.78)	21.5 (21.5)	8.3 (8.6)	–
$[Co(terpy)_2][BF_4]_2$	–	51.5 (51.5)	3.10 (3.17)	12.0 (12.0)	–	8.2 (8.4)
$[Ru(bpp)_2][BF_4]_2$	–	37.9 (37.9)	2.55 (2.60)	20.2 (20.1)	–	–
1a	0.97	41.0 (40.9)	2.70 (2.79)	21.3 (21.2)	8.4 (8.3)	0.3 (0.3)
1b	0.85	42.4 (42.3)	2.75 (2.84)	20.1 (20.0)	7.3 (7.2)	1.2 (1.3)
1c	0.76	43.3 (43.3)	2.80 (2.88)	19.2 (19.1)	6.3 (6.4)	1.9 (2.1)
2a	0.97	38.3 (38.3)	2.55 (2.62)	19.9 (19.8)	–	0.3 (0.3)
2b	0.85	39.9 (40.0)	2.65 (2.69)	19.0 (18.9)	–	1.2 (1.3)
2c	0.77	41.1 (41.0)	2.70 (2.73)	18.2 (18.2)	–	1.8 (1.9)

Single crystal structure of $[Ru(bpp)_2][BF_4]_2$

Single crystals of this compound were obtained by diffusion of diethyl ether vapour into a nitromethane solution of the complex. Experimental details for the structure determination are given in Table S2. One of the two BF_4^- anions is disordered over two sites, with a 0.7:0.3 occupancy ratio. The refined restraints B–F = 1.40(2) and F...F = 2.29(2) Å were applied to these disordered residues. All non-H atoms except for the minor anion disorder site were refined anisotropically, and H atoms were placed in calculated positions and refined using a riding model. CCDC 771524.

Table S2 Experimental details for the single crystal structure determination of $[Ru(bpp)_2][BF_4]_2$

Molecular formula	$C_{22}H_{18}B_2F_8N_{10}Ru$	μ (Mo-K_α) (mm^{-1})	0.661
M_r	697.15	*T* (K)	150(2)
Crystal class	Monoclinic	Measured reflections	22696
Space group	$P2_1$	Independent reflections	6364
a (Å)	8.5703(8)	R_{int}	0.062
b (Å)	8.6188(7)	$R(F)^a$	0.034
c (Å)	18.6937(16)	$wR(F^2)^b$	0.075
β (°)	97.706(6)	Goodness of fit	1.037
V ($Å^3$)	1368.4(2)	Flack parameter	−0.02(2)
Z	2		

$^aR = \Sigma[|F_o| - |F_c|] / \Sigma|F_o|$ $^bwR = [\Sigma w(F_o^2 - F_c^2) / \Sigma wF_o^4]^{1/2}$

Table S3 Selected bond lengths and angles in the crystal structure of $[Ru(bpp)_2][BF_4]_2$ (Å, °).

Ru(1)–N(2)	2.023(2)	Ru(1)–N(18)	2.022(3)
Ru(1)–N(9)	2.103(3)	Ru(1)–N(25)	2.095(3)
Ru(1)–N(14)	2.081(3)	Ru(1)–N(30)	2.079(3)
N(2)–Ru(1)–N(9)	78.41(11)	N(9)–Ru(1)–N(30)	92.54(11)
N(2)–Ru(1)–N(14)	78.35(11)	N(14)–Ru(1)–N(18)	101.06(11)
N(2)–Ru(1)–N(18)	178.26(19)	N(14)–Ru(1)–N(25)	92.16(12)
N(2)–Ru(1)–N(25)	103.82(14)	N(14)–Ru(1)–N(30)	90.29(12)
N(2)–Ru(1)–N(30)	99.83(13)	N(18)–Ru(1)–N(25)	77.82(13)
N(9)–Ru(1)–N(14)	156.73(10)	N(18)–Ru(1)–N(30)	78.51(13)
N(9)–Ru(1)–N(18)	102.13(11)	N(25)–Ru(1)–N(30)	156.23(10)
N(9)–Ru(1)–N(25)	94.46(11)		

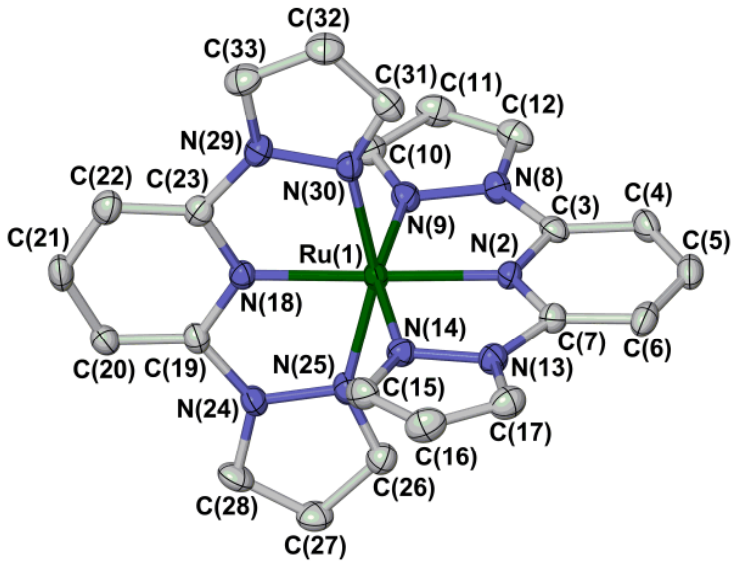

Fig. S2 View of the complex dication in $[Ru(bpp)_2][BF_4]_2$, showing the atom numbering scheme employed. All H atoms have been omitted for clarity, and thermal ellipsoids are at the 50% probability level.

$[Ru(bpp)_2][BF_4]_2$ is isostructural with $[Fe(bpp)_2][BF_4]_2$, and its crystal packing diagram is visually indistinguishable from those in Fig. S1.

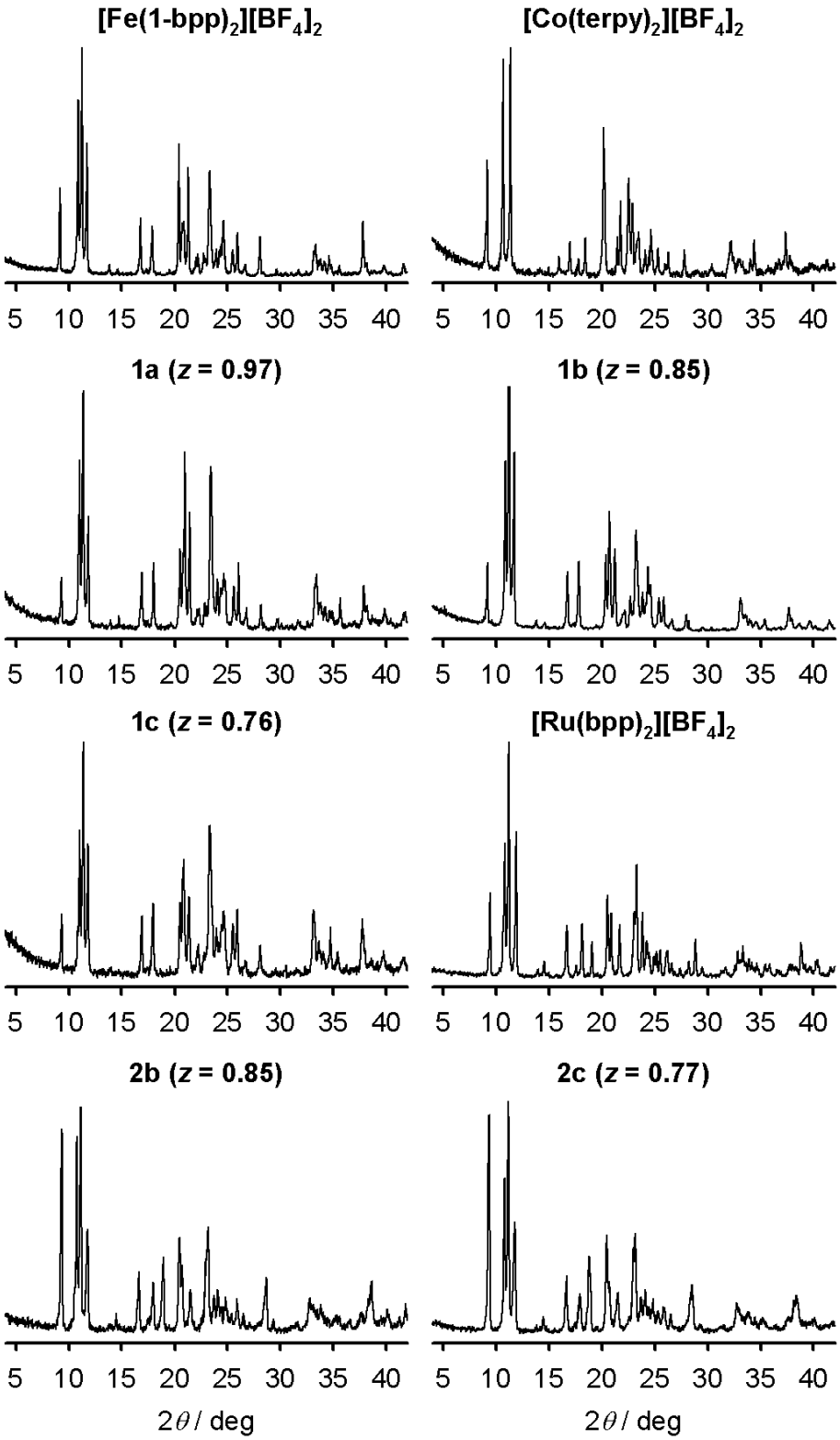

Fig. S3 Selected powder *X*-ray diffraction data from the compounds in this work at 298 K (λ = 1.5418 Å).

Table S4 Assignment of the electrospray (ES) mass spectra from $[M(bpp)_2][BF_4]_2$ (M = Fe and Ru), $[Co(terpy)_2][BF_4]_2$ and the solid solutions (Figure S4, next page). All peaks show correct isotopic distributions for their assigned molecular ions. Molecular ions of sodium- or formate-containing species arise from the sodium formate present in the ES carrier solution.

m/*z*	Intensity (%)[a]	Assignment
$[Fe(bpp)_2][BF_4]_2$		
565.1	11	$[^{56}Fe(bpp)_2(^{11}BF_4)]^+$
497.1	43	$[^{56}Fe(bpp)_2F]^+$
445.2	5	$[^{23}Na(bpp)_2]^+$
312.0	40	$[^{56}Fe(bpp)(O_2CH)]^+$
286.0	25	$[^{56}Fe(bpp)F]^+$
239.1	35	$[^{56}Fe(bpp)_2]^{2+}$
234.1	100	$[^{23}Na(bpp)]^+$
212.1	90	$[Hbpp]^+$
$[Ru(bpp)_2][BF_4]_2$		
611.1	13	$[^{102}Ru(bpp)_2(^{11}BF_4)]^+$
262.0	100	$[^{102}Ru(bpp)_2]^{2+}$
$[Co(terpy)_2][BF_4]_2$		
612.1	44	$[^{59}Co(terpy)_2(^{11}BF_4)]^+$
544.1	16	$[^{59}Co(terpy)_2F]^+$
311.0	9	$[^{59}Co(terpy)F]^+$
262.6	100	$[^{59}Co(terpy)_2]^{2+}$
Additional peaks seen in **1b** and **1c** only		
251.6	3-5[b]	$[^{59}Co(bpp)(terpy)]^{2+}$
250.1	3-4[b]	$[^{56}Fe(bpp)(terpy)]^{2+}$

[a]Intensities in the spectra of the pure complexes. The relative intensities of the same peaks in the spectra of **1a**-**1c** closely mirror those seen for the pure compounds (Fig. S4). [b]Intensity relative to the parent ion for $[^{59}Co(terpy)_2]^{2+}$ at *m*/*z* = 262.6.

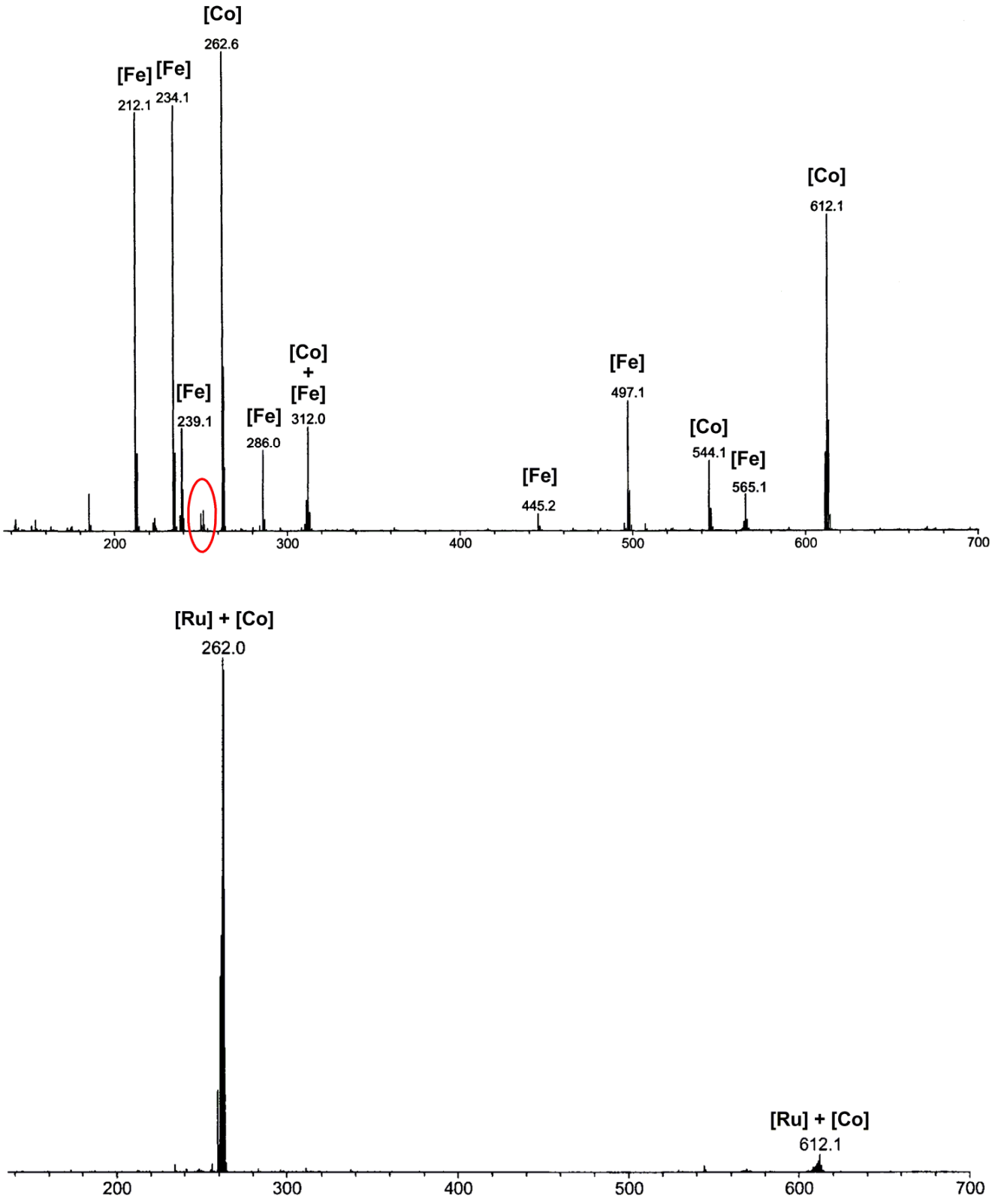

Fig. S4 Electrospray mass spectra of **1b** (top) and **2b** (bottom) from MeCN solution. Peaks are labeled according to whether they are also found in the spectra of pure $[Fe(bpp)_2][BF_4]_2$ ([Fe]), $[Ru(bpp)_2][BF_4]_2$ ([Ru]) or $[Co(terpy)_2][BF_4]_2$ ([Co]; Table S4).

The circled peaks in the spectrum of **1b** are assigned to the mixed-ligand species $[M(bpp)(terpy)]^{2+}$ (M = ^{56}Fe, *m*/*z* = 250.1 and M = ^{59}Co, *m*/*z* = 251.6). No peaks from $[M(bpp)(terpy)]^{2+}$ (M = ^{102}Ru, *m*/*z* = 273.1 and M = ^{59}Co, *m*/*z* = 251.6) are observed in the spectrum of **2b**.

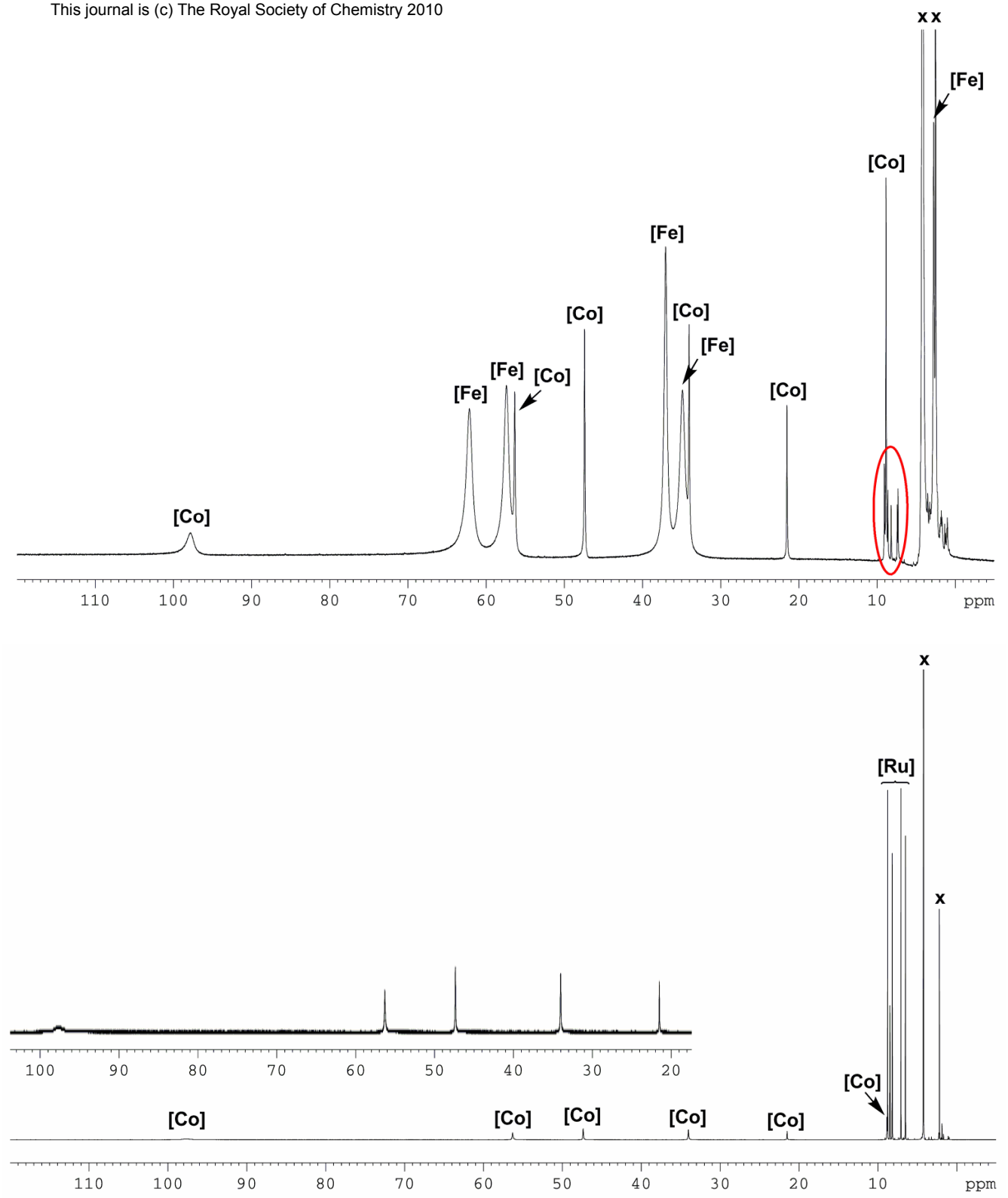

Fig. S5 ^{1}H NMR spectra of **1b** (top) and **2b** (bottom) at 298 K (CD_3NO_2, 300.1 MHz). Peaks are labeled according to whether they are also found in the spectra of pure $[Fe(bpp)_2][BF_4]_2$ ([Fe]), $[Ru(bpp)_2][BF_4]_2$ ([Ru]) or $[Co(terpy)_2][BF_4]_2$ ([Co]).

The circled peaks in the spectrum of **1b** correspond to a diamagnetic terpy-containing contaminent, that is not present in solutions of $[Co(terpy)_2][BF_4]_2$. The contaminent peaks are also not observed in freshly prepared mixtures of $[Fe(bpp)_2][BF_4]_2$ and $[Co(terpy)_2][BF_4]_2$, but grow in slowly over a period of hours.

Possible assignments of the contaminant include $[Fe(terpy)_2]^{2+}$ or, more likely, $[Co(terpy)_2]^{3+}$. It cannot be assigned as either of the mixed-ligand complexes $[M(bpp)(terpy)]^{2+}$ (M = Fe or Co), though (*c.f.* Fig. S4).

The peaks from $[Ru(bpp)_2][BF_4]_2$ are much more intense than those of $[Co(terpy)_2][BF_4]_2$ in the spectrum of **1b** because of the diamagnetism of the ruthenium compound.

Table S5 Predicted and observed values of $\chi_M T$ ($cm^3\ mol^{-1}\ K$) from high- and low-spin $[Fe(bpp)_2]_z[Co(terpy)_2]_{1-z}[BF_4]_2$ (**1a**-**1c**) and $[Ru(bpp)_2]_z[Co(terpy)_2]_{1-z}[BF_4]_2$ (**2a**-**2c**), based on the analytical compositions of the samples.

	z	Low-spin iron + low-spin cobalt (calc)	High-spin iron + high-spin cobalt (calc)	Observed $\chi_M T$ at: 5 K	100 K	400 K
1a	0.97	0.012	3.46	0.015	0.020	3.41
1b	0.85	0.060	3.32	0.057	0.077	3.26
1c	0.76	0.10	3.21	0.10	0.12	3.15

	z	Low-spin ruthenium + low-spin cobalt (calc)	Low-spin ruthenium + high-spin cobalt (calc)	Observed $\chi_M T$ at: 5 K	100 K	400 K
2a	0.97	0.012	0.069	0.015	0.017	0.064
2b	0.85	0.060	0.35	0.084	0.11	0.33
2c	0.77	0.092	0.53	0.13	0.19	0.53

The calculations use the following $\chi_M T$ values for the pure components of the solid solutions; high-spin $[Fe(bpp)_2][BF_4]_2$, = 3.5; low-spin $[Fe(bpp)_2][BF_4]_2$, 0; high-spin $[Co(terpy)_2][BF_4]_2$, 2.3; low-spin $[Co(bpp)_2][BF_4]_2$, 0.4; $[Ru(bpp)_2][BF_4]_2$, 0.

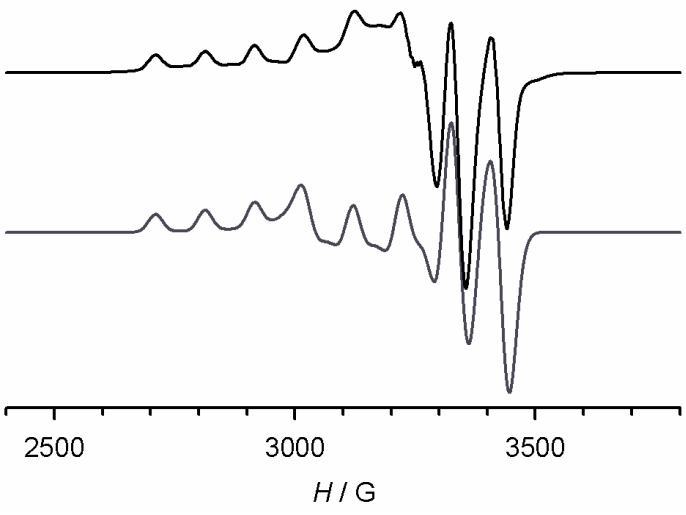

Fig. S6 Experimental (top) and simulated (bottom) *X*-band EPR spectrum of solid **1a** at 113 K (ν = 9.54 GHz). See the main text for the simulation parameters. Other EPR data are shown in Fig. S7, and in Fig. 2 of the main paper.

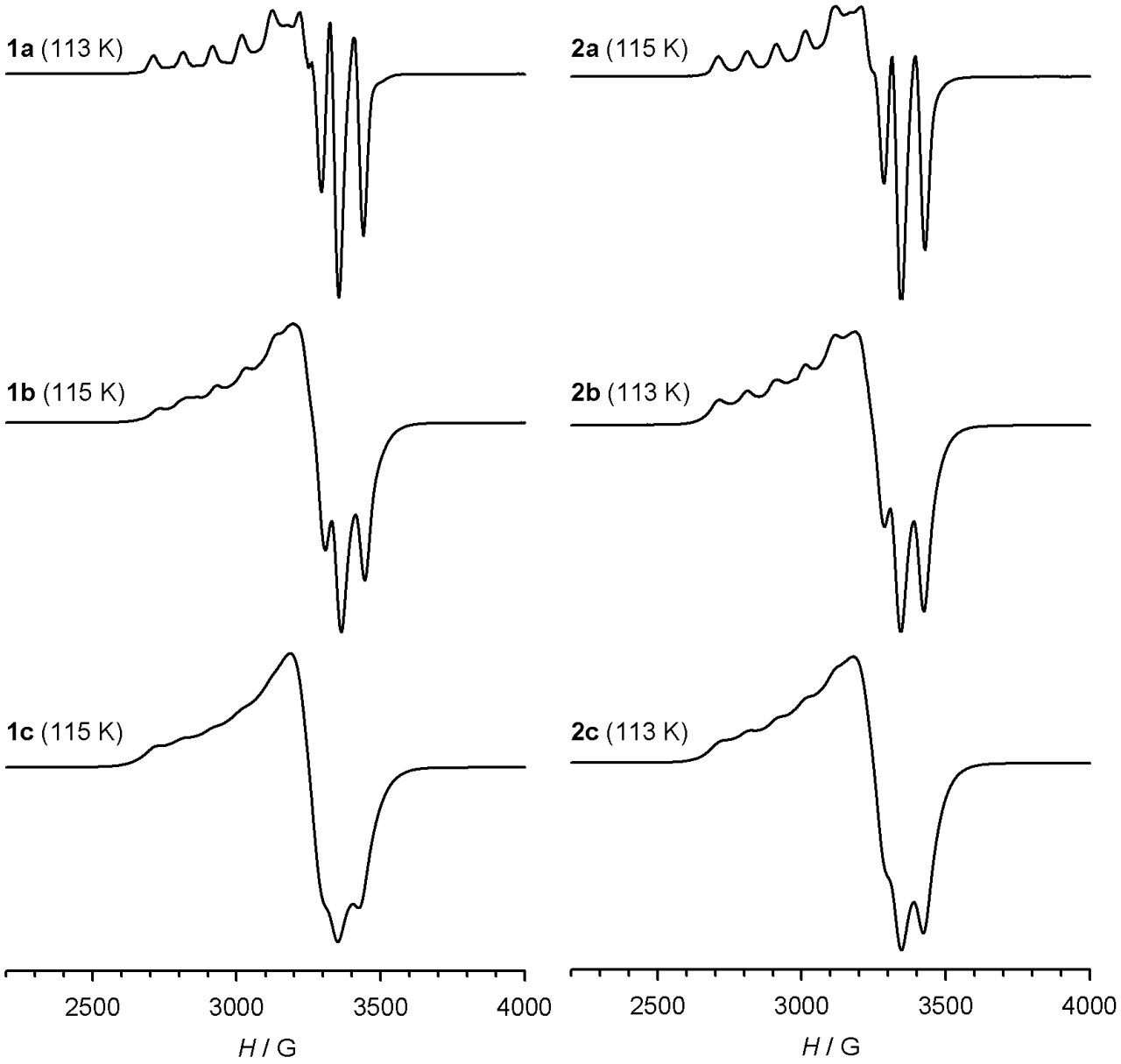

Fig. S7 Low temperature *X*-band powder EPR spectra of the solid solutions in this work as powder samples (ν = 9.54 GHz). A simulation of the spectrum of **1a** is shown in Fig. S6.